Pergamon

Atmospheric Environment Vol. 30, No. 7, pp. 1125–1135, 1996

1352-2310/96 $15.00 + 0.00

1352-2310(95)00335-5

A LABORATORY STUDY OF BUOYANT PLUMES IN LAMINAR AND TURBULENT CROSSFLOWS

PABLO HUQ and E. J. STEWART

College of Marine Studies and Center for Applied Coastal Research, University of Delaware, Newark, DE 19716, U.S.A.

(*First received* 14 *April* 1995 *and in final form* 21 *July* 1995)

Abstract—The results of laboratory experiments of buoyant plumes in crossflows are presented. Specific comparisons are made of plume evolution for laminar and weakly turbulent crossflows for otherwise identical flow parameters to establish that plume dilution rates differ significantly even for weakly turbulent crossflows. Decaying, grid-generated turbulence constituted the flow field of the weakly turbulent crossflow. Measurements comprised analyses of flow visualization, hot-film anemometry and conductivity probe data. Plume thicknesses and widths are found to be greater for turbulent crossflows, although they both grow as $x^{2/3}$ for laminar and turbulent crossflows. The effect of turbulence in the crossflow is to increase entrainment and dilution with the consequence of lower plume trajectories. It is found, relative to the values of dilution for buoyant plumes in a laminar crossflow, that dilutions of plumes in a weakly turbulent crossflow (with kinetic energy dissipation rates two orders of magnitude smaller than internal plume dissipation rates) were greater by 33%. Trajectories can be predicted by an integral model with a modified β, the entrainment coefficient, which relates the ratio of dissipation rates within and outside the plume.

Key word index: Atmospheric dispersion, laboratory modelling, integral plume models, plumes in crossflows, turbulence.

1. INTRODUCTION

Although numerous laboratory experimental studies have been conducted on buoyant plumes in crossflows, these experiments have been conducted primarily for laminar crossflows. Therefore, at present, the effects of external turbulence on the evolution of a buoyant plume in a crossflow are poorly understood (List, 1982; Schatzmann *et al.*, 1993; List and Duggan, 1994). The purpose of the present study is to examine, experimentally, the effects of a turbulent crossflow on the dynamics of a rising buoyant plume: comparison of the results of buoyant plumes in laminar crossflows, for otherwise identical flow parameters, discriminates the effects of turbulence. More specifically, an objective is to show that even for the weak perturbation of decaying, grid-generated turbulence there can be a large increase in dilution relative to the case of a buoyant plume in a laminar crossflow. In Section 2 we discuss buoyancy and momentum length scales, and briefly describe a simple integral plume model with whose predictions we compare our experimental results. The experimental apparatus is described in Section 3. Section 4 is the discussion of the results and is followed by the conclusions in Section 5. The focus of the present paper is to report the results of mean density measurements. A companion paper (Huq and Stewart, 1995) describes the analyses of density fluctuations for the flow fields of buoyant plumes in laminar and turbulent crossflows.

2. INTEGRAL PLUME MODEL ANALYSIS AND LENGTH SCALES

The principal factors governing the dynamics of buoyant plumes are buoyancy, drag and entrainment. Buoyancy causes the plume to rise; drag between the plume and its surroundings and crossflow distorts the geometry of the cross-section of the plume; entrainment of ambient fluid into the plume dilutes concentration and buoyancy. Numerous models have been developed to describe the dynamics of buoyant plumes. Principally, the focus has been to predict the evolution of the trajectory of the centerline of the buoyant plume. Following Morton *et al.* (1956), entrainment and drag coefficients are utilized in overall or integral balance equations for the conservation of mass, momentum and energy. The consensus of the model predictions of Fan (1967), Hoult *et al.* (1969), Ooms (1972), Hirst (1972), Hanna (1975), Briggs (1975), and Schatzmann (1979) is that sufficiently far downstream the plume centerline elevation z_c increases as the 2/3 power of the downwind distance x, and the plume radius R increases linearly with

centerline elevation. These findings have been confirmed by field and laboratory experiments (e.g. Slawson and Csanady, 1971; Manins, 1979; Alton *et al.*, 1993).

We use the simple integral model of Davidson (1989) which is also described by Alton *et al.* (1993). This model contains the empirical coefficients β and β_T. β is an entrainment constant that describes the turbulent growth of the plume, and β_T is a trajectory constant that describes a combination of the effects of entrainment and drag on the trajectory of the plume centerline. β and β_T are related as $\beta_T = (1+f)^{1/2}\beta$ with f an empirical factor. The typical value of the empirical factor f is taken as 1.3 together with values of $\beta = 0.4$ and $\beta_T = 0.6$ (Briggs, 1975; Davidson, 1989).

In the coordinate system shown in Fig. 1, the simple integral model predicts the height $z_c(x)$ of the mean plume centerline and the mean plume radius $R(x)$ as the following functions of distance, x, downstream of the plume source:

$$z_c(x) = \left[\frac{3}{\beta_T^2}\left(\tfrac{1}{2} l_B x^2 + l_M^2 x\right) + \left(\frac{R_0}{\beta}\right)^3\right]^{1/3} - \frac{R_0}{\beta} \quad (1)$$

$$R(x) = R_0 + \beta z_c(x) \quad (2)$$

In these expressions the buoyancy and momentum length scales are given in terms of the source conditions as

$$l_B = \frac{w_s R_s^2 g'}{\bar{U}^3} \quad (3)$$

$$l_M = R_s \frac{w_s}{\bar{U}}\left(\frac{\rho_s}{\rho_a}\right)^{1/2} \quad (4)$$

and the virtual plume source radius is

$$R_0 = R_s\left(\frac{w_s}{\bar{U}}\frac{\rho_s}{\rho_a}\right)^{1/2} \quad (5)$$

in which $\bar{U}$ is the mean ambient fluid speed, R_s is the plume source radius, w_s is the mean vertical speed of the plume effluents at the source, ρ_s is the density of the plume at the source, ρ_a is the ambient fluid density, and g' is the reduced gravity of the plume at the source.

We use the buoyancy length scale l_B in the presentation of experimental results. Note that equation (1) shows that for small values of x, where momentum effects dominate, $z_c \sim x^{1/3}$, and for larger values of x (i.e. $x > l_B$) when buoyancy dominates, $z_c \sim x^{2/3}$.

3. EXPERIMENTAL APPARATUS

Experiments were conducted in a plexiglass recirculating water tunnel that is 400 cm long, 40 cm deep and 25 cm wide. The flow in the tunnel is driven by centrifugal pumps from storage reservoirs. There is a free surface at the top of the water tunnel which allows the introduction of probes. Mesh screens, located upstream of the measurement section, reduce background turbulence to $w'/\bar{U} = 0.3\%$, where w' is the root-mean-square vertical velocity fluctuation and $\bar{U}$ is the mean velocity of the flow. Mean velocities are uniform aside from boundary layers at the bottom and side walls which grew to 1.5 cm at the downstream end of the tunnel. Mean velocities in the water tunnel were either 7.8 or 8.3 cm s^{-1}.

The plume source is a brass pipe with an internal diameter $\phi = 0.36$ cm. The exit of the source pipe is located 2.5 cm below the free surface. Flow through the source pipe is driven by a pump and monitored by a flowmeter. Source exit velocities, w_s, vary from 16 to 30 cm s^{-1} so that the source exit Reynolds number $w_s\phi/\nu$ varies from approximately 600 to 1000 where ν is the kinematic viscosity. Plume downwash in the lee of the source, which occurs when the value of the ratio $w_s/\bar{U}$ is below 1.5 (Snyder, 1981; Arya and Lape, 1990), is avoided as presently $2 < w_s/\bar{U} < 3.8$. Buoyancy is generated by adding brine to the storage reservoir of the plume source. The range of density difference $\Delta\bar{\rho}/\bar{\rho}$ is approximately 15–71 kg m^{-3} so that the range of $\Delta\bar{\rho}/\bar{\rho}$ varies between 0.0143 and 0.0658; the Froude number $F = (w_s/g'\phi)^{1/2}$ varied between $3.3 < F < 13.9$. Thus, values of the experimental parameters are similar to the previous studies of plumes in a laminar crossflow of Manins (1979) and Alton *et al.* (1993).

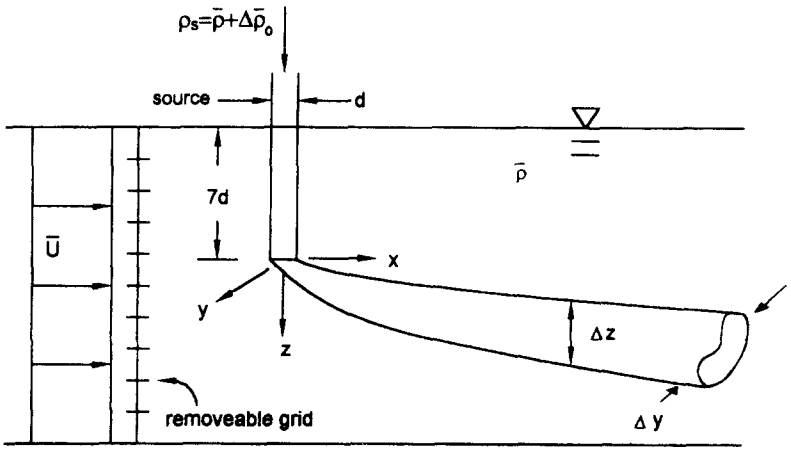

Fig. 1. Flow configuration and coordinate system. Removable turbulence generating grid is located 71d or 8.1M upstream of source (M and d are the grid mesh spacing and diameter of source, respectively).

Table 1. Values of experimental parameters

$\bar{U}$ (cm s^{-1})	w_s (cm s^{-1})	Q (cm^3 s^{-1})	ρ_s (g cm^{-3})	$\Delta\bar{\rho}/\bar{\rho}$	B (cm^4 s^{-3})	M (cm^4 s^{-2})	l_B (cm)	l_M (cm)	F
8.3	30	3.14	1.015	0.0143	43.99	95.54	0.0769	1.1776	13.36
8.3	21	2.20	1.015	0.0143	30.79	46.81	0.0539	0.8243	9.34
8.3	25	2.62	1.015	0.0143	36.66	66.34	0.0641	0.9814	11.13
8.3	30	3.14	1.034	0.0324	99.77	97.32	0.1745	1.1886	8.86
7.8	21	2.20	1.071	0.0658	141.89	49.40	0.2990	0.9011	4.36
7.8	30	3.14	1.071	0.0658	202.71	100.81	0.4272	1.2872	6.22
7.8	16	1.67	1.071	0.0658	108.11	28.67	0.2278	0.6865	3.32
7.8	30	3.14	1.014	0.0133	41.00	95.44	0.0864	1.2525	13.84
8.3	20	2.09	1.016	0.0155	31.80	42.50	0.0556	0.7855	8.55

Note that ρ, the ambient density, is 1.0005 g cm^{-3}. $F = (w_s/g'\phi)^{1/2}$ where $g' = (\Delta\bar{\rho}/\bar{\rho})g$. $M = (\bar{\rho}_s/\bar{\rho})Qw_s$. $B = g'Q$. $Q = w_s\phi^2/4$.

Values of the experimental parameters of the crossflow velocity $\bar{U}$, the source exit velocity w_s, the source volume flux Q and density ρ_s, the density ratio $\Delta\rho/\rho$, the buoyancy flux $B = Qg'$, the momentum flux $M = (\bar{\rho}_s/\bar{\rho})Qw_s$, the buoyancy and momentum length scales l_B and l_M are given in Table 1.

To generate turbulence in the crossflow a turbulence generating grid could be introduced into the tunnel when desired. The bi-plane grid comprises square plexiglass rods with sides of length $d = 0.64$ cm arranged in a mesh of spacing $M = 3.2$ cm. Thus, the value of mesh spacing to rod size is $M/d = 5$. The grid is located 26 cm upstream of the plume source pipe exit. Experiments are conducted with and without ambient turbulence in the crossflow; this is achieved by either running the tunnel with or without the grid, respectively. Values of the mesh Reynolds number $R_M = \bar{U}M/\nu$ were approximately 2700 for the experiments.

Two component (u, w) turbulent velocity measurements are obtained with a quartz-coated cylindrical x-film probe (Type TSI 1241-20W) operated at 2% overheat by an AN1003 anemometer unit. To correct for the small length (0.20 cm) to diameter (0.015 cm) ratio of the x-film probes yaw corrections with $k = 0.35$ are applied (Lawson and Britter, 1983).

An aspirating conductivity probe is used to measure the density field. This probe, which has a spatial resolution of 0.04 cm and a frequency response of 70 Hz, is driven in an AC bridge at 1 kHz. The x-film and conductivity probe are calibrated prior to each experiment in a nozzle and constant salinity baths, respectively. Data from the hot films and conductivity probes are recorded for 30 s, which had been ascertained to be sufficient for stable mean and rms intensity levels, and processed by an A–D interface and computer. Errors in the values of u' and w', the root-mean-square values of turbulent velocities, are typically 5%.

Red fluorescent Rhodamine dye is added to the plume source reservoir to visualize the flow. In addition to elevation views (x–z plane), a 45° overhead mirror provides plan views (x–y plane) of the plume. A grid of 30 × 10 cm is marked on the bottom and side of the tunnel to facilitate scaling from slides and photographs.

4. RESULTS AND DISCUSSION

4.1. *Flow visualization*

Figure 2 shows typical plan (x–y plane) and elevation (x–z plane) views of a plume discharging into a laminar crossflow. The plan view of Fig. 2a shows that the plume is approximately symmetrical about the $y = 0$ axis with the angle of spread being approximately 6°. The scale of convolutions of the visible boundary grows with distance x. For example, at $x = 50$ cm, typical convolutions were 1 cm in size; at $x = 100$ cm, convolutions were 3 cm. For this experiment the value of the length scale $l_B = 0.054$ cm. Figure 2b shows that the plume descends monotonically. The appearance of the structure of the upper and lower boundaries of the plume differs in that the upper boundary appears to be much less convoluted. Note that this is also the case for chimney discharges to the atmospheric boundary layer with, of course, top and bottom boundaries and the z coordinate axis reversed (Scorer, 1978, Fig. 10.7.2). The scale of the convolutions of the visible boundary in the x–z plane also grows with distance (e.g. at $x = 50$ cm), and vertical convolutions at the underside of the plume are typically 2 cm in size; by $x = 100$ cm, vertical convolutions grow to 3 cm.

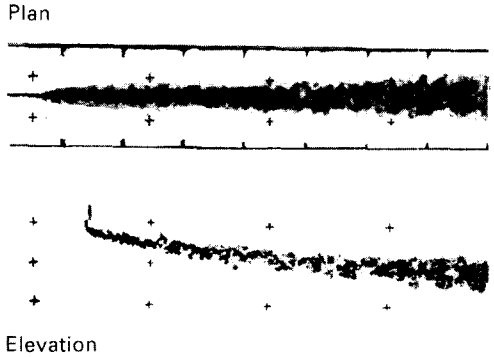

Fig. 2. Visualization of a buoyant plume in a laminar crossflow showing plan (x–y plane) and elevation (x–z plane) views; the crosses indicate the location of a grid of 30 cm in the x direction, and 10 cm in the y and z directions. The value of the buoyancy length scale $l_B = 0.054$ cm, see Table 1.

Figure 3 shows plan and elevation views for a plume discharging into a turbulent crossflow for flow parameters identical to Fig. 2. An effect of the presence of (external) turbulence in the crossflow is to increase average widths of the plume (e.g. in Fig. 2a at $x = 100$ cm, average width $\Delta y = 9.5$ cm without external turbulence). In comparison, Fig. 3a shows that the width at $x = 100$ cm is 11.5 cm with external

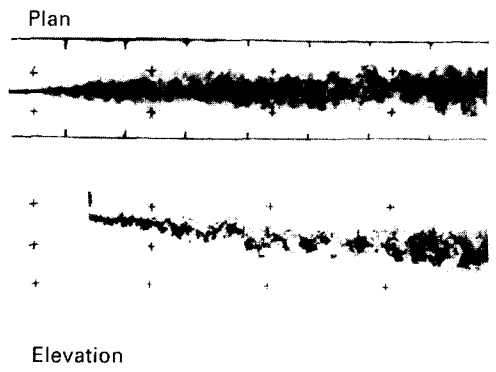

Fig. 3. Visualization of a buoyant plume in a turbulent crossflow. The symbols are the same as in Fig. 2. $l_B = 0.054$ cm.

turbulence. Second, the scale of the convolutions of the visible boundary is larger than those without a turbulent crossflow; in Fig. 2a at $x = 100$ cm the scale of convolutions is typically 3 cm, whereas with external turbulence they are approximately 4.5 cm in size. Visually the plumes appear similar in the x–y plane up to $x = 50$ cm, but farther downstream the convolutions are greater in scale for the case of the turbulent crossflow.

The effect of turbulence present in the crossflow is most manifest in the visualization of Fig. 3b. Here the plume is clearly more broken up than in Fig. 2b. This is so for the majority of the plume trajectory. A third effect of (external) turbulence in the crossflow is to increase the vertical extent of the plume (e.g. with turbulence at $x = 50$ cm, $\Delta z = 5.5$ cm and at $x = 100$ cm, $\Delta z = 6.9$ cm, this compares with laminar crossflow values of $\Delta z = 4.0$ and 6.2 cm at $x = 50$ and 100 cm, respectively).

4.2. *Plume geometry*

Detailed measurements are obtained using best-fit lines drawn through the visual edges of the plume on enlargements of the visualizations. The results, which are presented in Figs 4–7, describe the evolutions of the centerline trajectory z_c, the thickness Δz, the width Δy, and the aspect ratio $\Delta y/\Delta z$ of the plume.

The centerline of the plume is defined as being midway between the visual edges of the plume; this method of establishing the centerline is the geometric method of Alton *et al.* (1993). Figure 4 shows that the centerline, z_c, of the plume descends monotonically with distance x. Close to the source for distances up to $x/l_B \sim 30$, where the influence of the source momentum and geometry are significant, the trajectory evolves as $z_c \sim x^{1/3}$ in accord with equation (1). The effect of external turbulence on the mean trajectory is negligible for distances less than $x/l_B \sim 30$.

For larger distances $x/l_B > 30$, the laminar crossflow data approximately follow a $z_c \sim x^{2/3}$ evolution. This is in accord with equation (1) when $x \gg l_M$, and is also in agreement with the lab and field data of Manins (1979) and Weil (1988). Despite the scatter, Fig. 4 shows that external turbulence causes a small but significant decrease in plume centerline trajectory for $x/l_B > 30$. The centerline trajectories for a turbulent crossflow also follow an approximate $z_c \sim x^{2/3}$ evolution but with smaller values of z_c of about $10z/l_B$

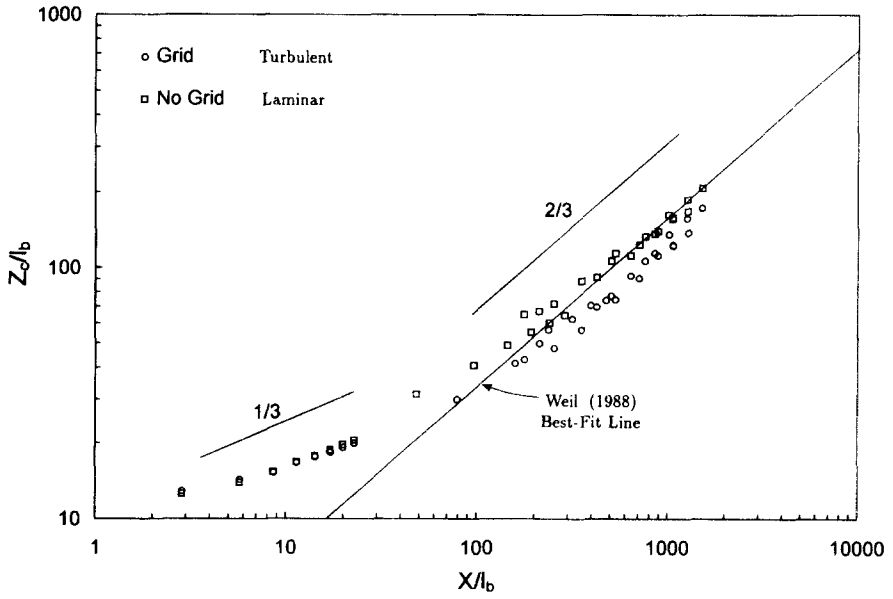

Fig. 4. Vertical rise of center of plume as a function of downwind distance with and without turbulence generating grid (i.e. turbulent and laminar crossflows). Indicated are 1/3 and 2/3 power-law slopes, and the best-fit line of Weil (1988) for various data.

at $x/l_B = 200$, and $40z/l_B$ at $x/l_B = 1000$. That the trajectories are higher for a laminar crossflow suggests that an effect of external turbulence is to enhance entrainment and dilution; this is demonstrated to be the case in Section 4.4. Also shown in Fig. 4 is the best-fit line of Weil (1988) for various lab and field experimental data for the evolution of z_c; the best-fit line also follows a $z_c \sim x^{2/3}$ evolution and is in good agreement with the present data for larger distances $x/l_B > 30$.

Figure 5 shows that with or without external turbulence $\Delta z \sim x^{2/3}$ for $x/l_B > 30$. For $x/l_B < 30$ there are negligible differences, but for $x/l_B > 30$ the plume thicknesses are greater with external turbulence; e.g. at $x/l_B = 200$, $\Delta z/l_B = 42$ and 29 with and without external turbulence, and at $x/l_B = 1000$, $\Delta z/l_B = 130$ and 92 with and without external turbulence. The present data for plume thickness Δz are in good agreement with the best-fit line for Δz data of Manins (1979) as is shown in Fig. 5.

Figure 6 shows that Δy also grows as $x^{2/3}$. The effect of external turbulence is to increase widths relative to the laminar crossflow case. For example, at $x/l_B = 200$, $\Delta y/l_B = 40$ and 33 with and without

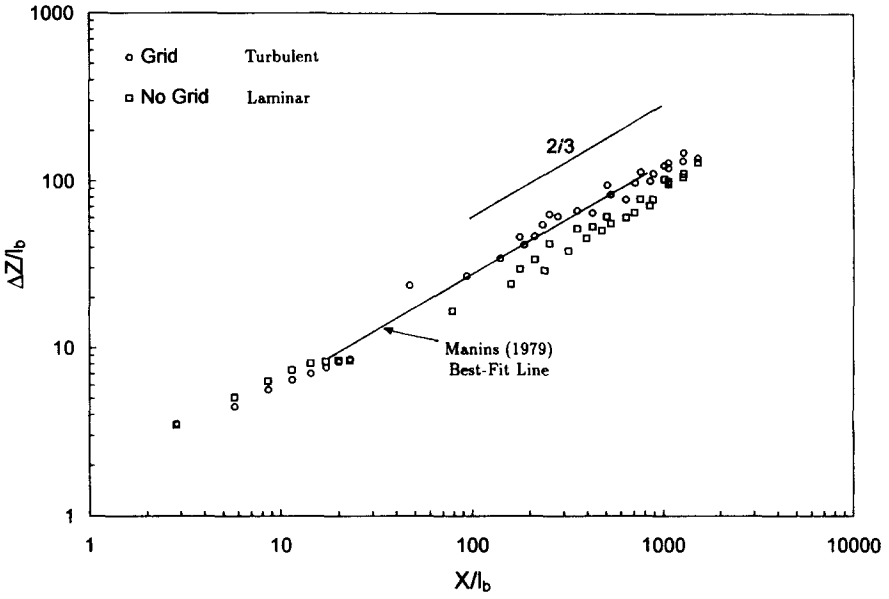

Fig. 5. Evolution of plume thickness with downwind distance for both turbulent and laminar crossflows. Indicated is a 2/3 power-law slope.

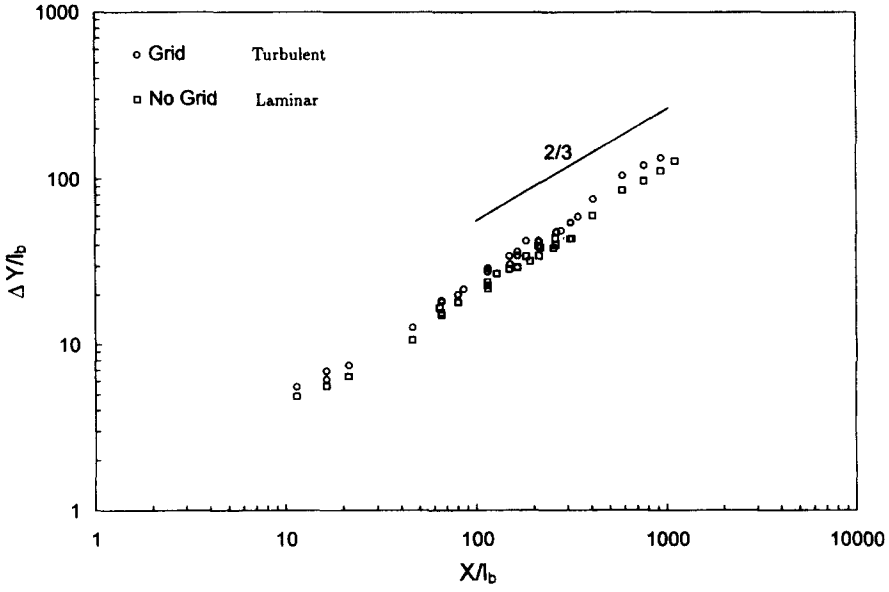

Fig. 6. Evolution of plume width with downwind distance for both turbulent and laminar crossflows. Indicated is a 2/3 power-law slope.

external turbulence, and at $x/l_B = 1000$, $\Delta y/l_B = 143$ and 120 with and without external turbulence. Evidently the effect of a turbulent crossflow on plume dimensions is similar as regards height and width in that the magnitudes of changes, and the manner of the evolution with distance x, are similar. That the quantities Δy and Δz evolve similarly suggests that the structure of the flow field evolves in a self-similar manner.

It is possible to evaluate the evolution of the aspect ratio (or ellipticity) of the plume by calculating the ratio of the width to height $\Delta y/\Delta z$ at various values of the longitudinal distance x. The results presented in Fig. 7 show that the aspect ratio of the plumes evolve with distance. At the source exit the aspect ratio is unity; the interaction of the discharge with the crossflow distorts plume geometry and leads to a double vortex structure with axial vorticity that is kidney-shaped (Sykes *et al.*, 1986; Needham *et al.*, 1988; Coelho and Hunt, 1989). Thus, in the vicinity of the plume source exit the aspect ratio is quickly distorted from an initially circular cross-section. Figure 7 shows that the aspect ratio changes slowly for large distances beyond $x/l_B > 600$.

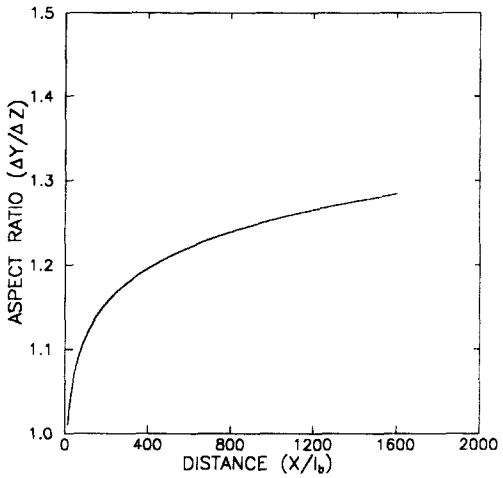

Fig. 7. Evolution of the aspect ratio with downwind distance for laminar crossflows. The curve is developed from best-fit lines to laminar crossflow data of Figs 5 and 6.

4.3. *Turbulence and dissipation rates*

A turbulent crossflow is generated by locating the turbulence generating grid in the crossflow upstream of the plume source exit. The resulting turbulence is thus decaying, grid-generated turbulence. The evolution of the turbulent velocity field downstream of the grid is shown in Fig. 8. For decaying, grid-generated turbulence both u' and w' decay with distance from the grid, and the decay is well approximated by the empirical formula

$$(u_i'/\bar{U})^2 = A_i\left(\frac{x}{M} - C\right)^{-N}, \quad i = 1, 2 \qquad (6)$$

where $u_1' = u'$, $u_2' = w'$. The values of the constants for the present data are $A_1 = 0.035$ for u', $A_2 = 0.027$ for w', $C = 3$, $N = 1.1$. Thus, the anisotropy ratio $w'/u' = 0.88$, a value which is characteristic of decaying, grid-generated turbulence (Bradshaw, 1971).

For grid-generated turbulence the rate of dissipation of turbulent kinetic energy, ε_A, is found from $\varepsilon_A = -\frac{3}{2}(d/dt)(u'^2) \approx -\frac{3}{2}\bar{U}(d/dx)(u'^2)$ and, using the above constants and differentiating (6), ε_A is given by

$$\varepsilon_A(x) = 0.058\,\frac{\bar{U}^3}{M}\left(\frac{x}{M} - 3\right)^{-2.1}. \qquad (7)$$

To calculate the dissipation rate in the plume it is necessary to determine the velocity of the plume. Using the relation between distance and time, $x = Ut$, we obtain the mean vertical speed $W(x)$ of the plume centerline as a function of downstream distance x by

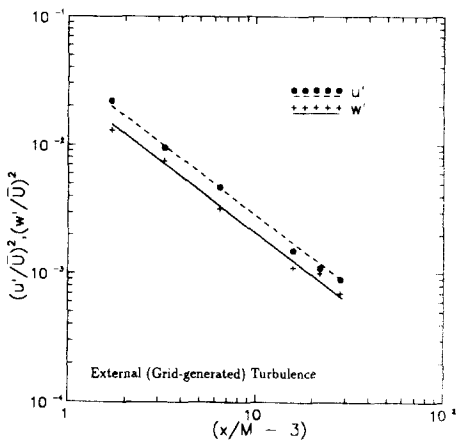

Fig. 8. Decay of turbulent velocity fluctuations u', w' for turbulence generating grid. Decay curves are of the form $(u_i/\bar{U})^2 = A(x/M - 3)^{-1.1}$, see equation (6).

differentiating equation (1):

$$W(x) = \frac{dz_c}{dt} = \bar{U}\frac{dz_c}{dx} = \bar{U}\left[\frac{1}{\beta_T^2}\left(l_B x + l_M^2\right)\right]\Big/\left[z_c(x) + \frac{R_0}{\beta}\right]^2. \qquad (8)$$

Following the dimensional arguments of Briggs (1975, 1984) we obtain an estimate of the mean turbulent dissipation rate $\varepsilon_P(x)$ of the plume turbulence as a function of x:

$$\varepsilon_P(x) = aW^3(x)/R(x) \qquad (9)$$

where the constant $a = 1.5$ [the standard value, but in any case should be some 0(1) value].

Comparisons of the dissipation rates of plume turbulence [given by equation (9)], and the dissipation rates of the external grid-generated turbulence [given

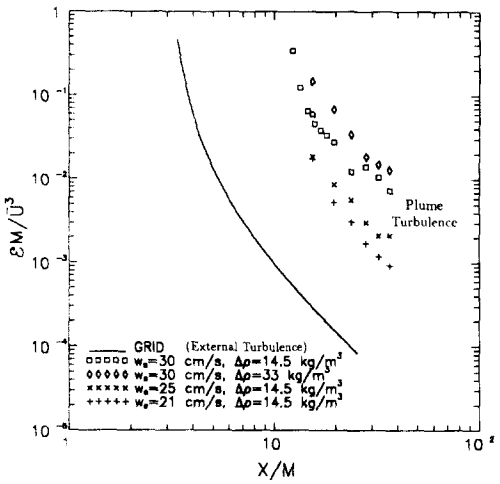

Fig. 9. Longitudinal/downwind evolution of nondimensional dissipation rates for turbulence generating grid, and typical cases of internally generated plume turbulence given by equations (9) and (7).

by equation (7)] are shown in Fig. 9 for various plumes. (Note that the dissipation rates for the grid and plume have been nondimensionalized by $M/\bar{U}^3$, and the abscissa by M.) Data are shown only for representative experiments in order to illustrate trends of increasing dissipation rates, ε_P, with increasing discharge velocity, w_s, and buoyancy difference, $\Delta\rho$. For all the experiments shown in Fig. 9 the internally generated plume dissipation rates are about two orders of magnitude greater at a given value of x; this is because the turbulence grid is located far upstream of the plume source exit (see Section 3). Thus, the relative magnitude of the perturbation of the turbulence in the crossflow may be considered to be weak.

4.4. *Mean density measurements*

Vertical transects of the mean density $\bar{\rho}$ through the plume centerline (i.e. $y/l_B = 0$) are shown in Fig. 10. Note that mean concentration $\bar{\rho}$ is nondimensionalized by the initial density difference at the source $\Delta\bar{\rho}_0$. Data are presented for three longitudinal locations (x/l_B = 177, 354 and 531) for both cases of plumes with and without external grid-generated turbulence. Figure 10 shows that (1) maximum concentrations $\bar{\rho}/\Delta\bar{\rho}_0$ decrease with increasing distance, (2) the z coordinate of the location of the peak concentration increases with distance x (i.e. the plume descends), (3) the mean concentrations without the grid are consistently greater than with the grid (i.e. the external turbulence enhances mixing), and (4) the z coordinate of the maximum concentration is greater for the case without external turbulence (i.e. the plume travels greater vertical distances for laminar crossflow). These trends are in accord with the results from flow visualization of Sections 4.1 and 4.2.

A plot of the evolution of centerline dilution ($\Delta\bar{\rho}_0/\bar{\rho}_{MAX}$) developed from the data of Fig. 10 for locations of maximum concentration is shown in Fig. 11. This is a striking illustration of the effects of external turbulence. It is clear that centerline dilutions are greater for the case of the plume with a turbulent crossflow. The weak perturbation of decaying grid-generated turbulence in the crossflow causes significant increases in the dilution; for a given value of x/l_B there is approximately 33% greater dilution. A second

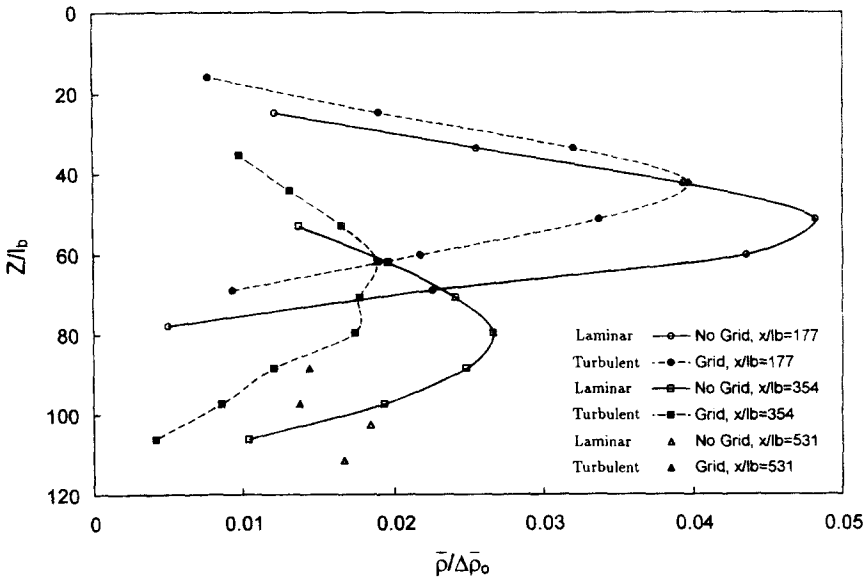

Fig. 10. Vertical profiles of mean density at plume centerline (i.e. $y = 0$) for buoyant plume for both laminar and turbulent crossflows. The value of buoyancy length scale $l_B = 0.055$ cm.

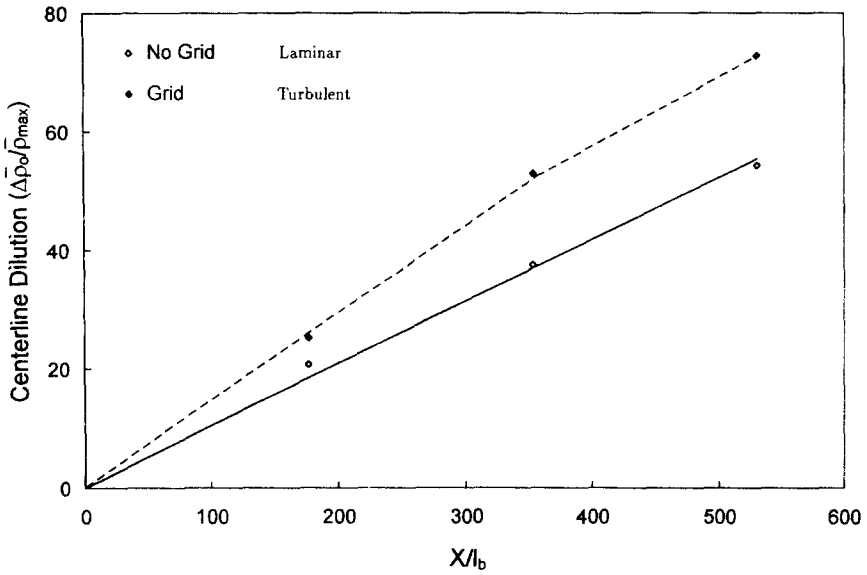

Fig. 11. Evolution of centerline dilution (i.e. at $y = 0$) with downwind distance developed from loci of maximum concentration from Fig. 12 for laminar and turbulent crossflow. Best-fit lines are drawn through data points.

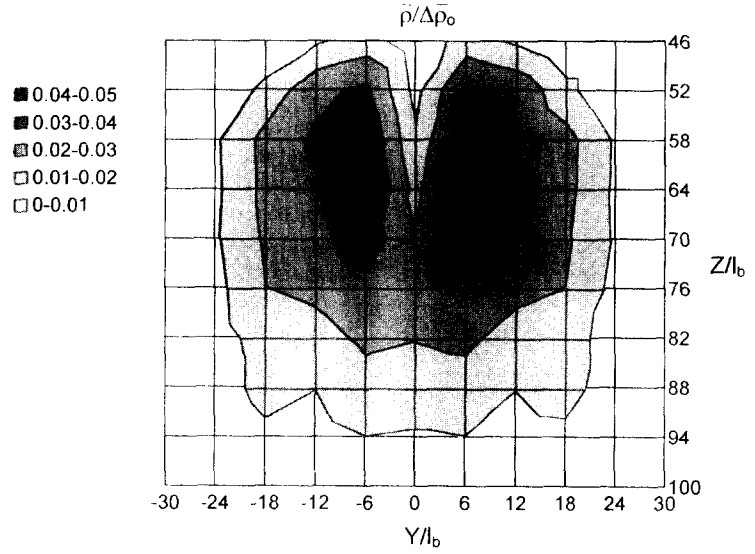

Fig. 12. Transverse section (y–z plane) at $x/l_B = 260$ of mean density field for laminar crossflow with $l_B = 0.077$ cm. Note that only data for values of $y \geqslant 0$ were obtained; data for negative values of y were generated by reflection.

point to note is the eventual large dilutions (> 50) for plumes in laminar and turbulent crossflows.

Contours of nondimensional mean density $\bar{\rho}/\Delta\bar{\rho}_0$ in the y–z plane are shown in Fig. 12. (The flow is into the sheet.) Contours are developed from high-resolution mapping with data points at every $6z/l_B$ and $6y/l_B$. Note that only data for positive y values are collected—data for negative y values are a mathematical reflection and are only shown to help interpretation. Similar to the data of Alton *et al.* (1993), it is evident that the structure of the plume comprises two relatively high-density cores. Second, the contours are not circular, but rather are approximately elliptical with a major to minor axis ratio of about three. Note that the aspect ratio of width to height ($\Delta y/\Delta z$) of the $\bar{\rho}/\Delta\bar{\rho}_0 = 0.01$ contour is about 1.0 in accord with the visualization data of Fig. 7 for $x/l_B = 260$. Third, note that the contours are generally inclined at 6–7° to the vertical axis. In contrast, for a similar flow configuration but without buoyancy forces Huq and Dhanak

(1995) find that concentration contours are not inclined. Finally, the contours are not uniformly spaced; the greater density of contours indicates that density gradients are greater at the top of the plume (i.e. smaller values of z/l_B).

4.5. *Comparison of trajectory with predictions of integral model*

The best-fit lines for both laminar and turbulent crossflow data describing the evolution of the transverse dimension of the plume are shown in Fig. 13. Best-fit lines are shown for Δz, Δy and R, where Δz is the plume thickness, Δy the plume width, and $R = (\Delta x \Delta y/\pi)^{1/2}$ the equivalent radius of the plume. The data show that the evolution of the transverse scale of the plume is linear, in agreement with equation (2). Values of the entrainment coefficient β are determined from the slopes of the best-fit lines of Fig. 13. The measured values of β for Δz, Δy and R are similar; differences in the values of β reflect the departure from a circular cross-section of the buoyant plume. (Recall that Fig. 7 showed that the value of the aspect ratio was greater than 1.0.) The values of β are in agreement with values obtained in previous studies; for example, Alton *et al.* (1993) found $\beta = 0.408$ and $\beta_T = 0.608$ for their (equivalent radius) data of a buoyant plume in a laminar crossflow.

Values of $\beta = 0.39$ and 0.61, corresponding to best fit slopes to equivalent radius data R for laminar and turbulent crossflows, are used to find best fits to the data of the longitudinal centerline evolution z_c. The centerline trajectories of all the plume experiments together with predictions of the integral plume model of equation (1) for the buoyancy-dominated regime ($x \gg l_M$) are plotted in Fig. 14. For the physical scales typical of laboratory experiments, the length, z_{pc} of the flow development zone (or potential core) in the vicinity of the source is a significant fraction of the measured trajectory heights. To allow for the fact that the potential core length z_{pc} is a significant fraction of the measured trajectory heights, the data of Fig. 13 include a correction for the potential core length. Following Fan (1967) and Alton *et al.* (1993), the potential core length is given empirically by

$$z_{pc} = 12.4 R_s \exp(-3.3\bar{U}/w_s). \tag{10}$$

And the total plume rise is corrected by adding z_{pc} to the rise predicted by equation (1). Comparison of the experimental data for the case of the laminar crossflow shows that the agreement with corrected integral model predictions with $\beta = 0.39$, $\beta_T = 0.55$ is good to within 20% over two decades of values of x/l_B. The data for the case of a turbulent crossflow also show agreement with corrected predictions to within 20% albeit with values of $\beta = 0.61$, $\beta_T = 0.86$. These values of combinations of β and β_T indicate a value of $f = 1.0$ for the empirical factor f which relates β and β_T as $\beta_T = (1+f)^{1/2}\beta$. This value of $f = 1.0$ is in approximate accord with the previous estimate of $f = 1.2$ of Alton *et al.* (1993). Note that the value of f is not dependent on whether the crossflow is laminar or turbulent in our experiment.

For the turbulent crossflow the increase in the value of β reflects greater entrainment rates and dilution. The increased dilutions arising from the presence of turbulence in the crossflow can be modeled by a modified entrainment coefficient β'. As a measure of the relative strengths of internally generated plume

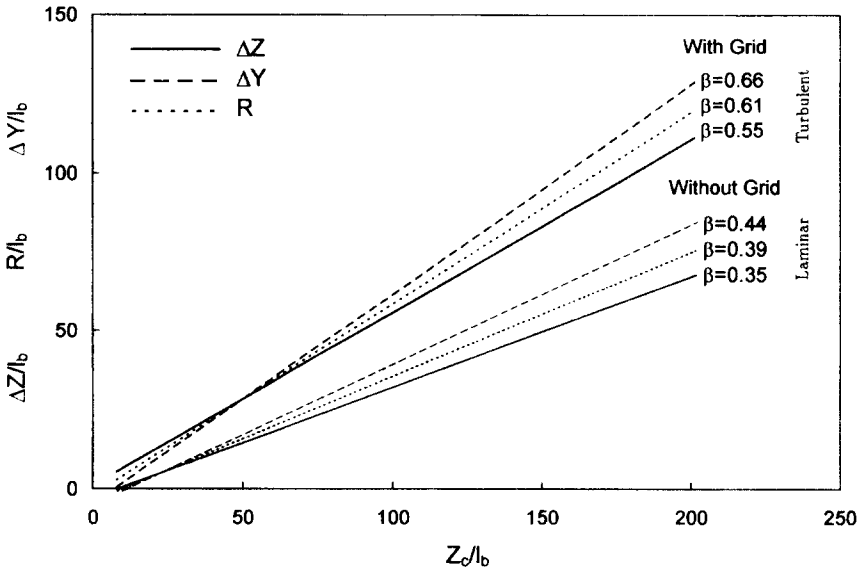

Fig. 13. Evolution of plume transverse scale with height. Best-fit lines are shown for the plume thickness Δz, the plume width Δy and an equivalent plume radius $R = (\Delta z \Delta y/\pi)^{1/2}$. Best-fit lines for both laminar and turbulent crossflow cases are shown. The values of β corresponding to slopes of best-fit lines are indicated.

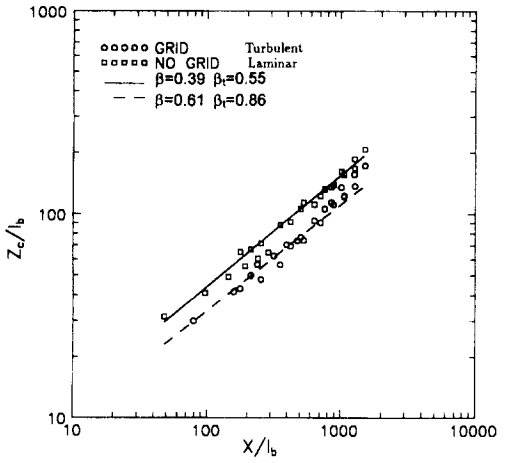

Fig. 14. Comparison of all experimental data of plume centerline trajectory with integral model [equation (1)]. Indicated are values of coefficients β and β_T for predictions using equation (1) for laminar and turbulent crossflows.

turbulence to external, decaying, grid-generated turbulence is expressed by the ratio of the dissipation rates ε_P and ε_A shown in Fig. 9, it may be anticipated that a modified entrainment coefficient, which accounts for the greater mixing due to the presence of external turbulence in the crossflow, will depend on the ratio $\varepsilon_A/\varepsilon_P$. Empirically we find that augmented entrainment rates for a turbulent crossflow depend on the ratio of plume and external dissipation rates ε_A and ε_P as

$$\beta' = \beta + (\varepsilon_A/\varepsilon_P)^N. \quad (11)$$

Our data of Fig. 9 yield a best-fit value of $N = 0.3 \pm 0.05$.

5. CONCLUSIONS

We have conducted a laboratory experimental investigation of the effects of a turbulent crossflow on a buoyant plume. Turbulence in the crossflow is generated by a turbulence generating grid which could be removed if desired. Comparison of the flow field of a buoyant plume, which resulted from a circular source discharging normal to the crossflow with and without the turbulence generating grid, discriminates the effects of turbulence in a crossflow.

From detailed analyses of flow visualization, hot-film anemometry and conductivity measurements of the velocity and density fields, we find that an effect of decaying, grid-generated turbulence, whose dissipation rates are approximately two orders of magnitude smaller than the internal plume turbulence dissipation rates, is to increase dilutions in the core of the buoyant plume by 33%. Plume trajectories are found to follow power laws of $z \sim x^{1/3}$ and $z \sim x^{2/3}$ for small and large values of x/l_B, respectively, for both laminar and turbulent crossflows. The experiments show that another effect of a turbulent crossflow is lower plume trajectories. For example, at a distance of $1000x/l_B$ from the plume source, trajectories are lower by $40z_c/l_B$. Plume depths and widths are found to evolve as $x^{2/3}$ for large values of x/l_B; it is also found that turbulence in the crossflow increases plume depths and widths.

Plume trajectories are predicted to within 20% by adopting reasonable values for β, the entrainment coefficient, of a simple integral plume model. Augmented dilutions due to the presence of external turbulence can be accounted for by a modified entrainment coefficient β' which depends on the ratio of internal plume and external (crossflow) turbulence dissipation rates $\varepsilon_A/\varepsilon_P$.

Acknowledgements—We thank Dr J. W. Rottman for critical discussions and Michael Meyer for invaluable help in the preliminary experiments. Financial support from the E. I. DuPont de Nemours, Inc. is gratefully acknowledged.

REFERENCES

Alton B. W., Davidson B. W. and Slawson P. R. (1993) Comparison of measurements and integral model predictions of hot water plume behavior in a crossflow. *Atmospheric Environment* **27A,** 589–598.

Arya S. P. S. and Lape J. F. (1990) A comparative study of the different criteria for the physical modeling of buoyant plume rise in a neutral atmosphere. *Atmospheric Environment* **24A,** 289–295.

Bradshan P. (1971) *An Introduction to Turbulence and its Measurement*. Pergamon Press, Oxford.

Briggs G. A. (1972) Discussion of chimney plumes in neutral and stable surroundings. *Atmospheric Environment* **6,** 507–510.

Briggs G. A. (1975) Plume rise predictions. In *Lectures on Air Pollution and Environmental Impact Analyses* (edited by Haughen D. A.), pp. 59–111. Amer. Met. Soc., Boston.

Briggs G. A. (1984) Plume rise and buoyancy effects. In *Atmospheric Science and Power Production* (edited by Randerson D.), pp. 327–366. U.S. Department of Energy DOE/TIC-27601, available from NTIS as DE84005177.

Coelho S. L. V. and Hunt J. C. R. (1989) The dynamics of the near field of strong jets in crossflows. *J. Fluid Mech.* **200,** 95–120.

Davidson G. A. (1989) Simultaneous trajectory and dilution predictions from a simple integral model. *Atmospheric Environment* **23,** 341–349.

Fan L. N. (1967) Turbulent buoyant jets into stratified on flowing ambient fluids. Report KH-R-15, W. M. Keck Laboratory, Cal. Tech, Pasadena, California.

Hanna S. R. (1975) Predicted and observed cooling tower plume rise and visible length at the John E. Amos power plant. *Atmospheric Environment* **10,** 1043–1052.

Hirst E. (1972) Buoyant jets with three-dimensional trajectories. *J. Hydraul. Div. Am. Soc. Civ. Engrs* **98,** 1999–2014.

Hoult D. P., Fay J. A. and Forney L. J. (1969) A theory of plume rise compared with field observations. *J. Air Pollut. Control Ass.* **19,** 585–590.

Huq P. and Dhanak M. R. (1995) The bifurcation of circular jets in crossflow. *Phys Fluids* (submitted).

Huq P. and Stewart E. J. (1995) Measurements of density fluctuations of buoyant plumes in turbulent crossflows. *Atmospheric Environment* (submitted).

Lawson R. E. and Britter R. E. (1983) A note on the measurement of transverse velocity fluctuations with heated cylindrical sensors at small mean velocities. *J. Phys. E. Sci. Instrum.* **16,** 563–567.

List E. J. (1982) In *Turbulent Buoyant Jets and Plumes* (edited by Rodi W.), pp. 1–68. Pergamon Press, Oxford.

List E. J. and Duggan R. (1994) Transition from jet plume dilution to ambient turbulent mixing. In *Recent Advances in the Fluid Mechanics of Turbulent Jets and Plumes* (edited by Davies P. A. and Valente Neves M. J.). Kluwer Academic Publishers, Dordrecht.

Manins P. C. (1979) Partial penetration of an elevated inversion layer by chimney plumes. *Atmospheric Environment* **13,** 733–741.

Morton B. R., Taylor G. I. and Turner J. S. (1956) Turbulent gravitational convection from maintained and instantaneous sources. *Proc. R. Soc. A* **234,** 1–23.

Needham D. J., Riley N. and Smith J. H. B. (1988) A jet in crossflow. *J. Fluid Mech.* **188,** 159–184.

Ooms G. (1972) A new method for the calculation of the plume path of gases emitted by a stack. *Atmospheric Environment* **6,** 899–909.

Schatzmann M. (1979) An integral model of plume rise. *Atmospheric Environment* **13,** 721–731.

Schatzmann M., Snyder W. H. and Lawson R. E. (1993) Experiments with heavy gas jets in laminar and turbulent cross-flows. *Atmospheric Environment* **27A,** 1105–1116.

Scorer R. S. (1978) *Environmental Aerodynamics.* Ellis Horwood, Chicester.

Slawson P. R. and Csanady G. T. (1971) The effects of atmospheric conditions on plume rise. *J. Fluid Mech.* **47,** 33–49.

Snyder W. H. (1981) Guideline for fluid modeling of atmospheric diffusion. Report EPA-600/8-81-009, 185 pp., Environmental Sciences Research Laboratory, U.S. Environmental Protection Agency, Research Triangle Park, North Carolina.

Sykes R. I., Lewellen W. S. and Parker S. F. (1986), On the vorticity dynamics of a turbulent jet in a crossflow. *J. Fluid Mech.* **168,** 393–413.

Weil J. C. (1988) Plume rise. In *Lectures on Air Pollution Modelling* (edited by Venkatram A. and Wyngaard J. C.), pp. 119–166. Amer. Met. Soc., Boston.